A multi-time-scale framework for state of energy and maximum available energy of lithium-ion battery under a wide operating temperature range.

CHEN, L, WANG, S., JIANG, H. and FERNANDEZ, C.

2024

A multi-time-scale framework for state of energy and maximum available energy of lithium-ion battery under a wide operating temperature range

Lei Chen[a], Shunli Wang[a,*], Hong Jiang[a], Carlos Fernandez[b]

[a]*School of Information Engineering, Southwest University of Science and Technology, Mianyang 621010, China;*

[b]*School of Pharmacy and Life Sciences, Robert Gordon University, Aberdeen AB10-7GJ, UK.*

Abstract: Lithium-ion batteries are one of the best choices as energy storage devices for self-powered nodes in wireless sensor networks (WSN) due to their advantages of no memory effect, high energy density, long cycle life, and being pollution-free after being discarded, ensuring that the sensor nodes maintain high power operation for a long time. An improved co-estimation framework for SOE and maximum available energy has been established, considering the problem of maximum available energy decay caused by temperature and battery charge-discharge rate, which can update the maximum available energy in real-time and reduce SOE errors caused by fixed energy values. A multi-timescale SOE and maximum available energy co-estimation framework is proposed to address the asynchronous and coupled characteristics of maximum available energy and SOE estimation, effectively reducing the algorithm's computational complexity. The proposed algorithm is experimentally verified according to the designed dynamic stress test conditions of lithium-ion batteries in WSN nodes. The experimental results show that smaller time scales can provide more accurate and reliable maximum available energy correction and higher SOE estimation accuracy, but the computational time cost is higher than that of larger time scales. To balance SOE estimation accuracy and algorithm computational complexity, the appropriate time scale should be selected based on the SOE estimation accuracy and time cost in practical battery management system working conditions.

Key words: Lithium-ion batteries; Bi-polarization fractional-order equivalent circuit model; State of energy; Maximum available energy; Multi-timescale;

***Corresponding author**: Shun-Li Wang. Tel: +86-15884655563. E-mail address: 497420789 @qq.com.

1. Introduction

The accurate estimation of the remaining energy of lithium-ion batteries provides a reference for maintaining the normal operation of nodes. The SOE of lithium-ion batteries cannot be directly measured, and a suitable model needs to be established to obtain it through external parameter measurement. The modeling methods for lithium-ion batteries mainly include electrochemical models, equivalent circuit models, and black box models [1]. The electrochemical model [2,3] establishes partial differential equations through charge diffusion and offset motion, which have clear physical meanings and high estimation accuracy. However, the computational complexity of partial differential equations is large, making it difficult to execute on microcontrollers. The black box model [4] does not consider the internal reaction mechanism of the battery and adopts data-driven algorithms to study the relationship between the output voltage and model input. This type of algorithm requires a large amount of training data, has high algorithm complexity, and the prediction results excessively rely on the accuracy of selected data, making it unsuitable for application to wireless sensor networks (WSN) nodes.

The equivalent circuit model (ECM) has a simple structure and is easy to implement, making it the most widely used state estimation algorithm currently. The common ECM models include the Rint model, Thevenin model [5], PNGV model [6], dual polarization equivalent circuit model [7], and fractional order equivalent circuit model (FOM) [8,9]. Reference [10] demonstrated through comparative analysis of ECM and FOM modeling methods that FOM modeling can fit the dynamic characteristic curve of batteries through continuously changing orders, better describing the physical characteristics of the model, and its modeling accuracy is higher.

The commonly used SOE estimation methods include direct voltage method[11] and open circuit voltage method [12], which are simple to operate but have low accuracy and dynamic range and are not suitable for online estimation. Data-driven algorithms [13,14] require a large amount of training data and are not suitable for WSN nodes to learn the characteristics of lithium-ion batteries by establishing data models or neural networks. The power integration method [15] is simple and direct in the calculation, but it is difficult to obtain the initial value, which is a commonly used method in WSN nodes. The Kalman filter in adaptive estimation methods [16] and its derivative algorithms [17,18] achieve SOE estimation by establishing a dynamic model of lithium-ion batteries and using Kalman filters to update and modify the state. This type of algorithm has reliable calculation results and can meet the requirements of real-time estimation.

Reference [19] proposed a universal model for online prediction of battery remaining capacity based on the coulomb counting method, which has better measurement accuracy than the direct voltage method. Reference [20] points out that the availability of battery energy, device drive cycle, and environmental conditions all have an impact on node lifespan. A new method for adaptive soc estimation based on Gaussian process regression in WSN is proposed, and the accuracy advantage of the model is verified by comparing with polynomial regression and support vector machine models. Reference [21] proposed a method based on voltage measurement to approximate the remaining energy of batteries. The prediction accuracy of this method is verified through experiments under temperature fluctuations, battery aging, and different load conditions. However, this result relies on high-precision measurement equipment to obtain measured voltage values under different conditions, ignoring the nonlinear changes in battery terminal voltage, which can have a significant impact on the results. Reference [22] developed the dual filtering algorithm to establish the online model-based estimator for SOE and established the total available energy capacity model to track the change of the maximum available energy. However, the choice to update the energy change at each sampling interval will bring a huge computational burden to BMS. Reference [23] proposed a dual estimation framework for SOE and maximum available energy based on a variable multi-timescale, which verified the accuracy and robustness of the SOE and maximum available energy co-estimation through presetting the energy threshold as the time scales but missed verification of the co-estimation performance under low-temperature conditions. In general, the discharge performance is very stable at room temperature and low discharge rate. The calculation of the remaining energy is less difficult and more accurate, but the drastic changes in the load current under actual operating conditions will result in a significant reduction in maximum available energy [24].

Therefore, establishing a highly reliable equivalent modeling method and a highly applicable SOE estimation method is the primary task for energy storage applications [25]. This is a complex task, as the maximum usable capacity of lithium-ion batteries will fluctuate to a certain extent with the charging and discharging rate, environmental temperature, and cyclic aging [26,27]. In simple operating conditions (such as room temperature, low magnification, etc.), the parameters of lithium-ion batteries are very stable, making it easy to obtain high-precision state estimation values through calculations [28-30]. However, the complexity of actual operating conditions (such as temperature, current, humidity, power changes, etc.) can lead to frequent changes in measurable parameters of batteries. Thus, how to obtain more accurate SOE values under complex and variable operating conditions is currently a research difficulty.

2. Mathematical analysis

2.1. Equivalent modeling

The use of ideal capacitors in ECM makes it difficult to describe varying degrees of capacitive reactance radians, which can lead to a decrease in model accuracy[31]. The fractional calculus using fractional order impedance elements such as CPE and Walburg to describe capacitive reactance arc under non-ideal conditions, to fit the EIS curve of lithium-ion batteries well and improve the accuracy of the model. The large increase of charge transfer impedance at low temperatures will result in severe energy loss, a temperature-varying factor is added to FOM to improve the temperature adaptability. The temperature-varying fractional-order equivalent circuit model (TV-FOM) is established as shown in Fig. 1.

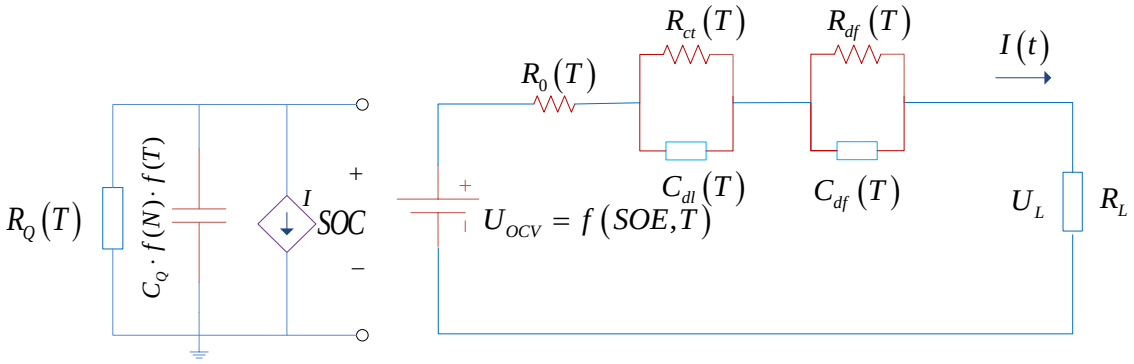

Fig. 1. Temperature-varying fractional-order equivalent circuit model

U_{OCV}(SOE, T) is the open-circuit voltage, C_Q is defined as a function of the nominal capacity Q_{nom}, C_{dl} and C_{df} are the element parameters of the capacitance model, and the fractional order is expressed as α, β. U_{cf} represents the partial voltage at the parallel connection of R_{ct} and C_{dl}, and U_{df} represents the partial voltage at the parallel connection of R_{df} and C_{df}. According to the electrochemical principle, the impedance form of C_{dl} and C_{df} is shown in Eq. (1).

$$\begin{cases} Z_{CPE_{dl}} = \dfrac{1}{C_{dl} S^{\alpha}} \\ Z_{CPE_{df}} = \dfrac{1}{C_{df} S^{\beta}} \end{cases} \quad \text{.....(1)}$$

According to Kirchhoff's law of voltage and current, the discretized state space equations of the polarization

voltage and terminal voltage of the circuit can be obtained as shown in Eq. (2).

$$\begin{cases} \begin{bmatrix} SOE(k) \\ U_{cf}(k) \\ U_{df}(k) \end{bmatrix} = \begin{bmatrix} 1 & 0 & 0 \\ 0 & -\dfrac{\Delta T^{\alpha}}{R_{ct}(T)C_{dl}(T)} & 0 \\ 0 & 0 & -\dfrac{\Delta T^{\beta}}{R_{df}(T)C_{df}(T)} \end{bmatrix} \begin{bmatrix} SOE(k-1) \\ U_{cf}(k-1) \\ U_{df}(k-1) \end{bmatrix} + \begin{bmatrix} \dfrac{\eta \Delta T U}{E_n(T)} \\ \dfrac{T^{\alpha}}{C_{dl}(T)} \\ \dfrac{T^{\beta}}{C_{df}(T)} \end{bmatrix} I_{k-1} - \begin{bmatrix} 0 \\ \sum_{j=1}^{k} \omega_j^{\alpha} U_{cf}(k-j) \\ \sum_{j=1}^{k} \omega_j^{\beta} U_{df}(k-j) \end{bmatrix} + \omega_{k-1} \\ U_L(k) = U_{OCV}(T, SOE) - [0 \quad 1 \quad 1][SOE(k) \quad U_{cf}(k) \quad U_{df}(k)]^T - R_0(T) I + v_k \end{cases} \quad \text{.....(2)}$$

2.2. Parameter identification

The variable double-order fractional-order forgetting factor recursive least square (VD-FOFFRLS) is used to achieve online identification of resistance capacitance parameters and fractional order, using temperature and SOE as variable factors to improve the accuracy of terminal voltage prediction. The impedance transfer function of FOM can be obtained as shown in Eq. (3).

$$\frac{U_{OCV}(s) - U_L(s)}{I(s)} = \frac{R_{ct}(T,Z)}{R_{ct}(T,Z)C_{dl}(T,Z)s^{\alpha(T,Z)} + 1} + R_0(T,Z) + \frac{R_{df}(T,Z)}{R_{df}(T,Z)C_{df}(T,Z)s^{\beta(T,Z)} + 1} \quad \text{.....(3)}$$

Simplify by defining Eq. (4).

$$\begin{cases} [a_1 \ a_2 \ a_3] = [\alpha(T,Z) \quad \beta(T,Z) \quad \alpha(T,Z) + \beta(T,Z)] \\ [b_1 \ b_2 \ b_3] = \begin{bmatrix} R_{ct}(T,Z)C_{dl}(T,Z) \\ R_{df}(T,Z)C_{df}(T,Z) \\ R_{ct}(T,Z)C_{dl}(T,Z)R_{df}(T,Z)C_{df}(T,Z) \end{bmatrix} \\ [c_0 \ c_1 \ c_2 \ c_3] = \begin{bmatrix} R_0(T,Z) + R_{ct}(T,Z) + R_{df}(T,Z) \\ R_{ct}(T,Z)C_{dl}(T,Z)\left(R_0(T,Z) + R_{df}(T,Z)\right) \\ R_{df}(T,Z)C_{df}(T,Z)\left(R_0(T,Z) + R_{ct}(T,Z)\right) \\ R_0(T,Z)R_{ct}(T,Z)C_{dl}(T,Z)R_{df}(T,Z)C_{df}(T,Z) \end{bmatrix} \end{cases} \quad \text{.....(4)}$$

y (k) is the difference between the open circuit voltage and the terminal voltage at time k. Combined with the G-L definition, Eq. (5) can be approximated as a linear regression equation.

$$y(k) + \sum_{j=1}^{3} b_j D^{a_j} y(k) = c_0 I(k) + \sum_{j=1}^{3} c_j D^{a_j} I(k) \quad \text{.....(5)}$$

According to the definition of fractional calculus:

$$\begin{cases} D^{a_j} y(k) = T^{-a_j} y(k) + T^{-a_j} \sum_{j=1}^{N} (-1)^j \binom{a_j}{j} y(k-j) \\ D^{a_j} I(k) = T^{-a_j} I(k) + T^{-a_j} \sum_{j=1}^{N} (-1)^j \binom{a_j}{j} I(k-j) \end{cases} \quad \text{.....(6)}$$

The fractional order calculus is historic and memorable. N is the number of historical data points involved in the historical calculation and contains all historical information from past moments. The computational complexity of the system continues to increase as N increases. Considering the accuracy requirements and the principle of short-term memory, it is necessary to choose a suitable memory length to truncate the data length N

during the calculation. Eq. (6) can be expanded as:

$$y(k)+b_1\left(y(k)-a_1y(k-1)+y(k)^{\Sigma a_1}\right)+b_2\left(y(k)-a_2y(k-1)+y(k)^{\Sigma a_2}\right)+\cdots$$

$$b_3\left(y(k)-a_3y(k-1)+y(k)^{\Sigma a_3}\right)=c_0I(k)+c_1\left(I(k)-a_1I(k-1)+I(k)^{\Sigma a_1}\right)+\cdots \quad (7)$$

$$c_2\left(I(k)-a_2I(k-1)+I(k)^{\Sigma a_2}\right)+c_3\left(I(k)-a_3I(k-1)+I(k)^{\Sigma a_3}\right)$$

Among them:

$$\begin{cases} y(k)^{\Sigma a_1}=T^{-a_1}\sum_{j=2}^{l}(-1)^j\binom{a_1}{j}y(k-j) \\ y(k)^{\Sigma a_2}=T^{-a_2}\sum_{j=2}^{l}(-1)^j\binom{a_2}{j}y(k-j) \\ y(k)^{\Sigma a_3}=T^{-a_3}\sum_{j=2}^{l}(-1)^j\binom{a_3}{j}y(k-j) \end{cases} \leftrightarrow \begin{cases} I(k)^{\Sigma a_1}=T^{-a_1}\sum_{j=2}^{l}(-1)^j\binom{a_1}{j}I(k-j) \\ I(k)^{\Sigma a_2}=T^{-a_2}\sum_{j=2}^{l}(-1)^j\binom{a_2}{j}I(k-j) \\ I(k)^{\Sigma a_3}=T^{-a_3}\sum_{j=2}^{l}(-1)^j\binom{a_3}{j}I(k-j) \end{cases} \quad (8)$$

Assuming:

$$\begin{cases} A(i)=\sum_{j=1}^{3}b_jT^{-a_j} \\ B(i)=\sum_{j=1}^{3}c_jT^{-a_j} \end{cases} \quad (9)$$

The linear regression equation of the FOM model is obtained by simplifying and organizing:

$$y(k)=\frac{-A(1)}{1+A(0)}y(k-1)-\frac{\tau_1}{1+A(0)}y(k)^{\Sigma a_1}-\frac{\tau_2}{1+A(0)}y(k)^{\Sigma a_2}-\cdots$$

$$\frac{\tau_1\tau_2}{1+A(0)}y(k)^{\Sigma a_3}+\frac{c_0+B(0)}{1+A(0)}I(k)+\frac{B(1)}{1+A(0)}I(k-1)+\cdots \quad (10)$$

$$\frac{\tau_1(R_0+R_2)}{1+A(0)}I(k)^{\Sigma a_1}+\frac{\tau_2(R_0+R_1)}{1+A(0)}I(k)^{\Sigma a_2}+\frac{\tau_1\tau_2R_0}{1+A(0)}I(k)^{\Sigma a_3}$$

Where $y(k)$ denotes the system output vector at time k, $\boldsymbol{\varphi}(k)$ denotes the system data vector at time k, and $\boldsymbol{\theta}(k)$ denotes the system parameter vector to be identified at time k.

$$\begin{cases} \boldsymbol{y}(k)=\boldsymbol{\varphi}(k)^T\boldsymbol{\theta}(k)+\boldsymbol{e}(k) \\ \boldsymbol{\varphi}(k)^T=\left[y(k-1)\ \ y(k)^{\Sigma a_1}\ \ y(k)^{\Sigma a_2}\ \ y(k)^{\Sigma a_3}\ \ I(k)\ \ I(k-1)\ \ I(k)^{\Sigma a_1}\ \ I(k)^{\Sigma a_2}\ \ I(k)^{\Sigma a_3}\right]^T \\ \boldsymbol{\theta}(k)=\left[a_0\ \ a_1\ \ a_2\ \ a_3\ \ b_0\ \ b_1\ \ b_2\ \ b_3\ \ b_4\right] \end{cases} \quad (11)$$

The parameter vector for the case of minimum system error vector is derived according to the forgetting factor recursive least squares.

$$\begin{cases} \hat{\boldsymbol{\theta}}(k)=\hat{\boldsymbol{\theta}}(k-1)+\boldsymbol{K}(k)\boldsymbol{e}(k) \\ \boldsymbol{e}(k)=\boldsymbol{Y}(k)-\boldsymbol{\varphi}^T(k)\hat{\boldsymbol{\theta}}(k-1) \\ \boldsymbol{K}(k)=\boldsymbol{P}(k-1)\boldsymbol{\varphi}(k)[\boldsymbol{\varphi}^T(k)\boldsymbol{P}(k-1)\boldsymbol{\varphi}(k)+\lambda]^{-1} \\ \boldsymbol{P}(k)=\lambda^{-1}[\boldsymbol{I}-\boldsymbol{K}(k)\boldsymbol{\varphi}^T(k)]\boldsymbol{P}(k-1) \end{cases} \quad (12)$$

$\hat{\boldsymbol{\theta}}(k)$ represents the estimated parameters to be identified at the current moment, $\hat{\boldsymbol{\theta}}(k-1)$ represents the estimated parameters to be identified at the previous moment. The estimated parameters are corrected by the product of the gain and the prediction error at the current moment to obtain the parameter vector for the FOM model with the minimum system error vector. Further derivation of the online identification parameters of the model is shown in Eq. (13).

$$\begin{cases} a_0 = \dfrac{a\tau_1 + b\tau_2 + (a+b)\tau_1\tau_2}{1+\tau_1+\tau_2+\tau_1\tau_2} \\ a_1 = -\dfrac{\tau_1}{1+\tau_1+\tau_2+\tau_1\tau_2} \\ a_2 = -\dfrac{\tau_2}{1+\tau_1+\tau_2+\tau_1\tau_2} \\ a_3 = -\dfrac{\tau_1\tau_2}{1+\tau_1+\tau_2+\tau_1\tau_2} \\ b_0 = \dfrac{R_0+R_1+R_2+\tau_1(R_0+R_2)}{1+\tau_1+\tau_2+\tau_1\tau_2} \\ \quad + \dfrac{\tau_2(R_0+R_1)+\tau_1\tau_2R_0}{1+\tau_1+\tau_2+\tau_1\tau_2} \\ b_1 = \dfrac{-a\tau_1(R_0+R_2)-b\tau_2(R_0+R_1)}{1+\tau_1+\tau_2+\tau_1\tau_2} \\ \quad + \dfrac{-(a+b)\tau_1\tau_2R_0}{1+\tau_1+\tau_2+\tau_1\tau_2} \\ b_2 = \dfrac{\tau_1(R_0+R_2)}{1+\tau_1+\tau_2+\tau_1\tau_2} \\ b_3 = \dfrac{\tau_2(R_0+R_1)}{1+\tau_1+\tau_2+\tau_1\tau_2} \\ b_4 = \dfrac{\tau_1\tau_2R_0}{1+\tau_1+\tau_2+\tau_1\tau_2} \end{cases} \Rightarrow \begin{cases} R_0 = -\dfrac{b_4}{a_3} \\ R_{ct} = -\dfrac{b_3}{a_2} - R_0 \\ R_{df} = -\dfrac{b_2}{a_1} - R_0 \\ \tau_1 = \dfrac{a_3}{a_2} \\ \tau_2 = \dfrac{a_3}{a_1} \\ \alpha = \dfrac{a_0(b_3+b_4)-b_1(a_2+a_3)}{b_2(a_2+a_3)-b_3(a_1+a_3)+b_4(a_2-a_1)} \\ \beta = \dfrac{a_0(b_2+b_4)-b_1(a_1+a_3)}{b_3(a_1+a_3)+b_4(a_1-a_2)-b_2(a_2+a_3)} \end{cases} \quad \text{.....(13)}$$

3. A novel combined estimation method for SOE and SOC with maximum available energy prediction

3.1. ADFOEKF based SOE and SOC co-estimation on the micro time-scale

The SOE is a numerical value that describes the remaining energy of the battery, which refers to the ratio of the remaining energy to the rated energy under certain charging and discharging rates and temperature conditions. Unfortunately, the traditional definition ignores the influence of terminal voltage change and maximum available energy change on the estimated results. The actual energy of the battery is the product of the actual capacity and voltage, and the capacity is equal to the integral of discharge current and discharge time, so the power output of the lithium-ion battery is mainly determined by the voltage and instantaneous current.

In working conditions, the power integration method is usually used for SOE estimation. The terminal voltage is an unstable factor, and energy characteristics experiments have shown that the charging and discharging rate,

temperature, and cycle times can cause dynamic changes in terminal voltage and maximum available energy. As the discharge process progresses, the voltage will gradually decrease with the decrease of battery charge, and there will be a rapid decrease in voltage at the end of the discharge. The energy characteristic experiments have shown that both charge-discharge rate and temperature can cause dynamic changes in voltage and maximum available energy values. It can be seen that the changes in voltage are closely related to the changes in the maximum available energy. The improved SOE is defined by the power integration method, and the discretization equation is shown in Eq. (14).

$$SOE(k+1) = SOE(k) + \frac{I(k)U(k)\Delta T}{E_n(I,T)} \quad (14)$$

Where SOE (k) is the energy value at time k, k is the sampling time, and E_n (I, T) is the maximum available energy, which is a fitting function of current rate and temperature, representing the variation values under different working conditions. According to the definition equation of SOC and SOE, the relationship between SOC and SOE can be obtained. The discrete state space equation is established as shown in Eq. (15):

$$\begin{cases} SOE(k+1) = SOE(k) + \dfrac{I(k)U(k)\Delta T}{E_n(I,T)} \\ U(k) = \dfrac{\left(SOE(k+1) - SOE(k)\right)\cdot E_n(I,T)}{\left(SOC(k+1) - SOC(k)\right)\cdot C_Q(I,T)} \end{cases} \quad (15)$$

The adaptive dual fractional-order extended Kalman filter algorithm (ADFOEKF) is used to realize the co-estimation of SOC and SOE. One Kalman filter is used to estimate SOC, and the other Kalman filter is used to estimate SOE based on SOC estimation results.

3.2. AEKF based maximum available energy prediction on macro time-scale

The battery parameters and state parameters have asynchronous time-varying characteristics, the state parameters have micro time-scale characteristics, and the model parameters have macro time-scale characteristics and are strongly related to the battery state parameters. The expression of the maximum available energy E_n is derived from the power definition equation of SOE, as shown in Eq. (16).

$$E_n(I,T) = -\frac{\int_k^{k+\Delta T} I_t U_t dt}{SOE_{k+\Delta T} - SOE_k} \quad (16)$$

Eq. (16) shows that an accurate SOE estimation can be obtained when the interval between two SOEs is long enough, which is difficult to achieve in practical environments. A fourth-order AEKF based on OCV correction is proposed to predict the maximum available energy E_n and realize the co-estimation for SOE and maximum available energy.

The micro-timescale SOE is updated at each sampling, and if the macro-timescale E_n is updated at each sampling, it will increase the operating cost. Therefore, it is necessary to choose an appropriate macro time scale to determine whether to update the maximum available energy. Assuming k and n represent the micro time scale of the state variable and the macro time scale of the parameter vector, respectively. L represents the macro time

scale transformation threshold, which means that the E_n is updated and estimated at every L sampling time point. [$E_{n,L}$ $U_{OCV,L}$ $U_{cf,L}$ $U_{df,L}$] is selected as the state variable, and the fourth-order AEKF is adopted to predict the maximum available energy. The second-order fractional-order discrete state space equation is established shown in Eq. (17).

$$\begin{cases} E_{n,L} = E_{n,L-1} + r \\ U_{OCV,L} = U_{OCV,L-1} + \dfrac{d(SOE,T)}{dSOE} \cdot \dfrac{I_{L-1} U_{L-1}}{E_{n,L}} \\ U_{cf,L} = U_{cf,L-1} \exp\left(-\dfrac{\Delta T}{C_{dl,L} R_{ct,L}} \right) + I_{L-1} R_{ct,L} \left[1 - \exp\left(-\dfrac{\Delta T}{C_{dl,L} R_{ct,L}} \right) \right] \\ U_{df,L} = U_{df,L-1} \exp\left(-\dfrac{\Delta T}{C_{df,L} R_{df,L}} \right) + I_{L-1} R_{df,L} \left[1 - \exp\left(-\dfrac{\Delta T}{C_{df,L} R_{df,L}} \right) \right] \\ U_L = U_{OCV,L}(SOE) - U_{cf,L} - U_{df,L} - I_L R_{0,L} \end{cases} \quad \text{.....(17)}$$

Consider $E_{n,L}$ as a constant within a single cycle of charging and discharging for lithium-ion batteries. If the sampling time k is an integer multiple of L, the optimal estimate of $E_{n,L}$ at the macroscopic time scale is updated, indicating the completion of a microscopic time scale cycle within the macroscopic time scale. If the sampling time k is not an integer multiple of L, the current value of $E_{n,L}$ is kept unchanged and the process continues back for the estimation of the state parameters at the next sampling time on the microscopic time scale. Therefore, SOE estimates need to be estimated and updated on micro time scales and E_n needs to be predicted and revised on macro time scales.

3.3. A multi-timescale framework for SOE and maximum available energy

The multi-timescale framework for state of energy and maximum available energy mainly includes fourth modules: online parameter identification module based on VD-FOFFRLS, micro-timescale SOE estimation module based on ADFOEKF, macro-timescale $E_{n,L}$ estimation module based on AEKF, and multi-time scale judgment module.

Firstly, the VD-FOFFRLS realizes the online identification of the model parameters and the online correction of the OCV. Secondly, the ADFOEKF module uses the identification parameters to realize the SOE estimation. Thirdly, according to the predicted SOE results and OCV data, the AEKF can further update the fixed maximum available energy when the time scale reaches a predetermined value. Finally, for multi-time scale judgment, SOE estimation needs to be estimated and updated at the micro time scale, while $E_{n,L}$ needs to be predicted and corrected at the macro time scale. The implementation process of the co-estimation for SOE and maximum available energy prediction based on the multi-timescale is shown in Fig. 2.

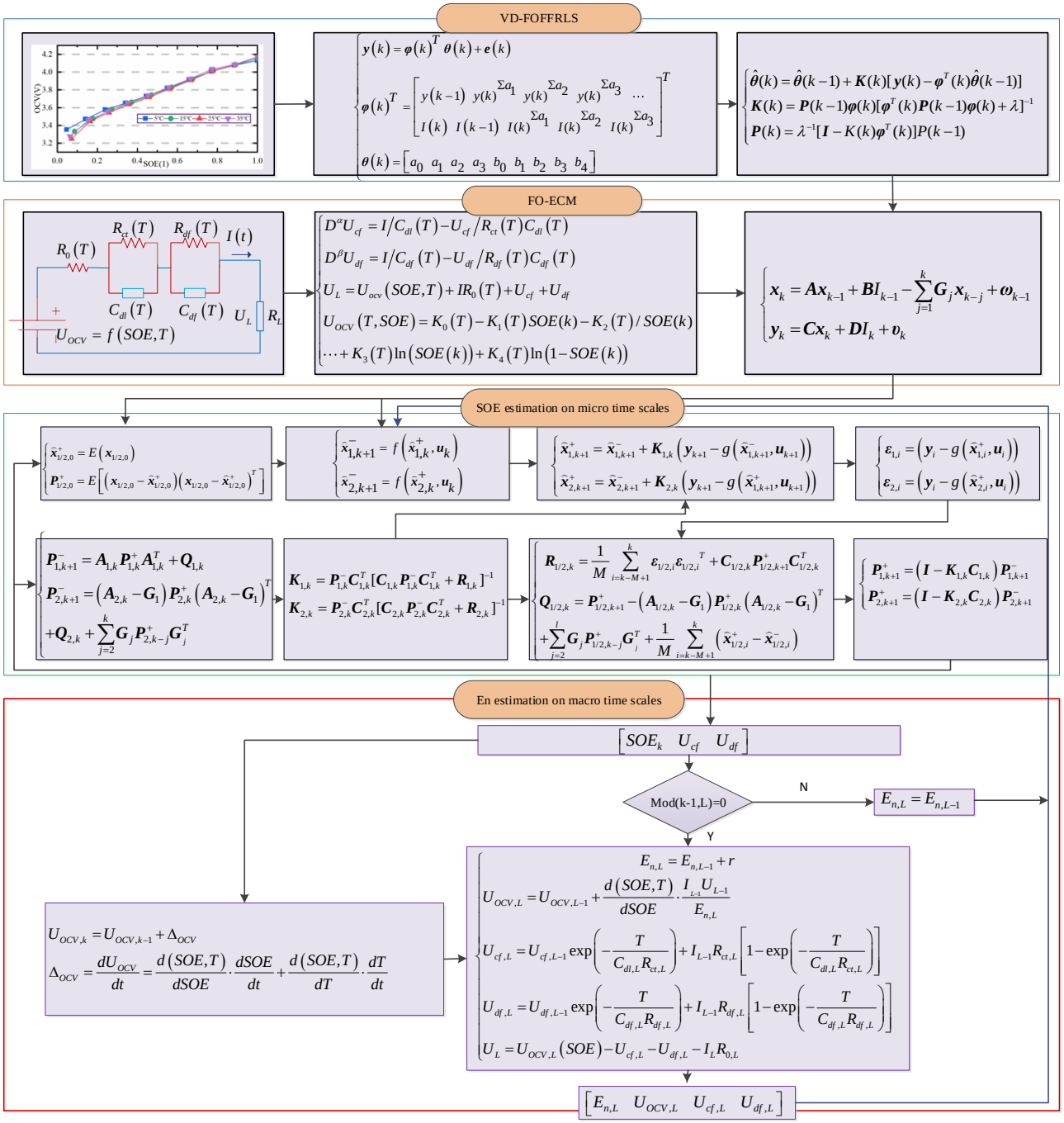

Fig.2. The flow chart of the multi-timescale framework for SOE and maximum available energy

4. Experimental analysis

4.1. Analysis of operating characteristics

Due to the discontinuous characteristics of photovoltaic energy harvesting in photovoltaic WSN, the ESS needs to store excess energy and release it when the power generation is insufficient to meet the load demand at night or on rainy days. The operating process of the lithium-ion battery is divided into five stages, the shutdown stage, the soft start stage, the normal charging stage, the intermittent energy supplement stage, and the intermittent energy supply stage. The operating condition represents the load power supply of the node under different weather conditions, which is related to the energy collection topology, working mode of the energy storage unit, and energy consumption model. Six typical operating conditions of nodes are designed, as shown in Tab. 1.

Tab. 1 Operating condition design

Operating condition	Actual conditions			
	Weather condition	Energy harvesting	Energy storage	Energy consumption
CS	Continuous Sunny	Autonomous energy supply	Supplementary power	Periodicity
CS1	Continuous Sunny	Autonomous energy supply	Supplementary power	Periodicity and randomness
CR	Continuous Rainy	Supplementary energy supply	Mainly powered	periodicity
CR1	Continuous Rainy	Supplementary energy supply	Mainly powered	Periodicity and randomness
SR	More sunny and less rainy	Mixed energy supply	Supplementary power	periodicity
SR1	Less sunny and more rainy	Mixed energy supply	Mainly powered	Periodicity and randomness

CS and CS1 correspond to continuous sunny days, and the energy required by the load is supplied directly by the energy harvesting device and supplemented by lithium-ion batteries. CR and CR1 correspond to continuous rainy days, the energy harvesting unit cannot obtain energy from the environment and can only use lithium-ion batteries as the main energy source. SR and SR1 correspond to alternating sunny and rainy days, the energy harvesting device and the storage device alternately supply power to the load, and the energy harvesting device is preferentially used to supply power to the load. Our previous work[32] has shown the current and voltage diagrams under six operating conditions.

4.2. Experimental operating conditions

Based on the working modes of the energy collection unit, energy storage unit, and energy consumption unit of the WSN node, representative DST conditions under different temperatures are designed from the energy supply unit module to simulate the discharge conditions. The experimental process is shown in Fig. 3.

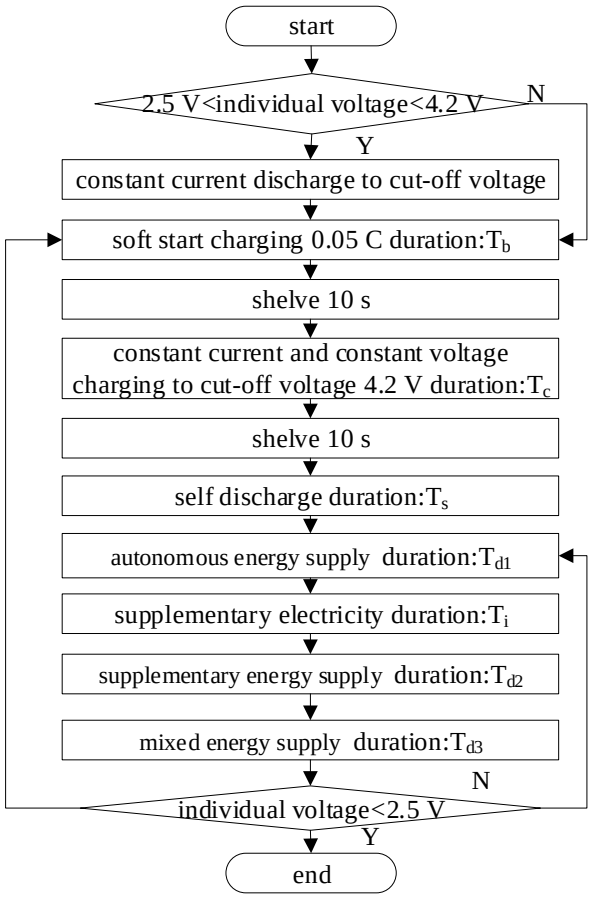

Fig.3. The flow chart of experimental design for working conditions

The experimental platform includes high-rate charge and discharge test equipment, 4.8Ah lithium-ion batteries, a host computer, and a high-low temperature control box. The battery placed in the control box is charged and discharged through the high-rate charge and discharge test equipment, and the host computer records the experimental data. By customizing the steps through the upper computer software, analyzing the working mode and state transfer mechanism of each module, and designing DST operating conditions under different temperatures and aging. The experimental data under different temperatures, charge-discharge rates, and cycle times are achieved through temperature settings and process step settings.

5. Results and Verification

5.1. Co-estimation prediction results of SOE and maximum available energy

The lithium-ion battery of WSN nodes is affected by different charging and discharging combinations of loads, and its working process is in a variable current state, resulting in a change in the maximum available energy. the polarization effect of the battery is increased in high-rate discharge, leading to the battery voltage quickly reaching the discharge cutoff voltage. However, there is still a portion of the actual capacity that has not been released, which is manifested as a decrease in the energy value that can be released. On the other hand, the total energy released increases at low discharge rates, while the total energy released gradually decreases with the increase of current. Six typical operating conditions at different temperatures are selected to verify the maximum available energy following effect under variable current and temperature conditions.

The influence of different time scales on co-estimation accuracy for SOE and maximum available energy must be comprehensively considered due to the strong interaction. The co-estimation accuracy and convergence time are used as indicators to evaluate the performance of the co-estimation framework with three different macro time scales, and the time scales L=10, L=30, and L=100 are selected to update the maximum available energy.

(1) L=10

The choice of different time scales will affect the update frequency of macro timescale and micro timescale. The micro timescale SOE is updated at each sampling time, while the maximum available energy E_n at the macro timescale is only updated when the macro timescale conversion threshold is reached. Select different time scales to update the maximum available energy to verify the adaptability of the joint algorithm under different time scales. Fig. 4 shows the SOE and maximum available energy co-estimation results and their estimation errors under different operating temperatures with L=10.

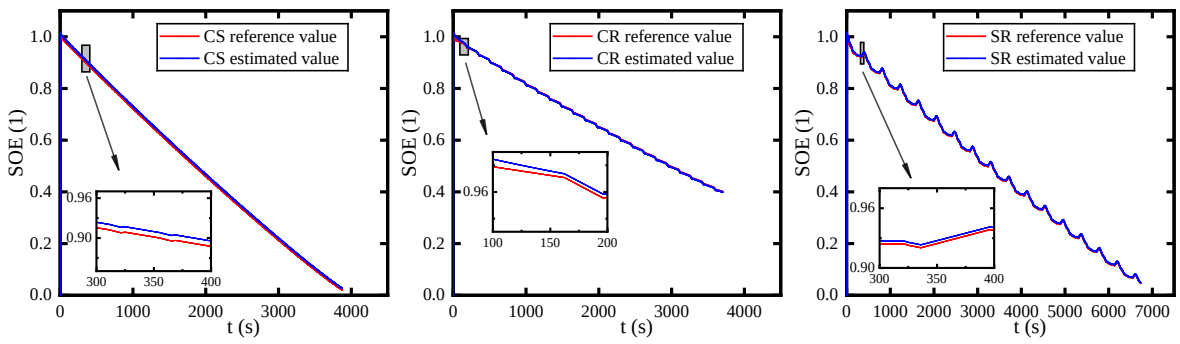

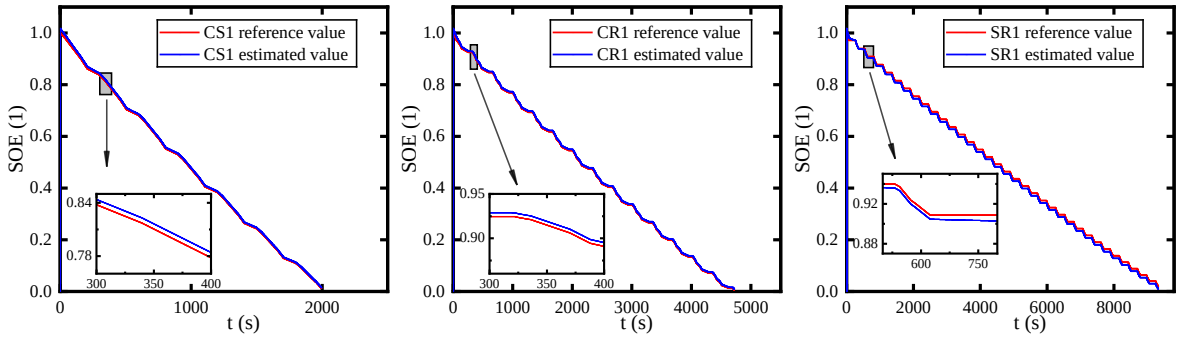

Fig. 4. (a) SOE and maximum available energy co-estimation results under 35 ℃

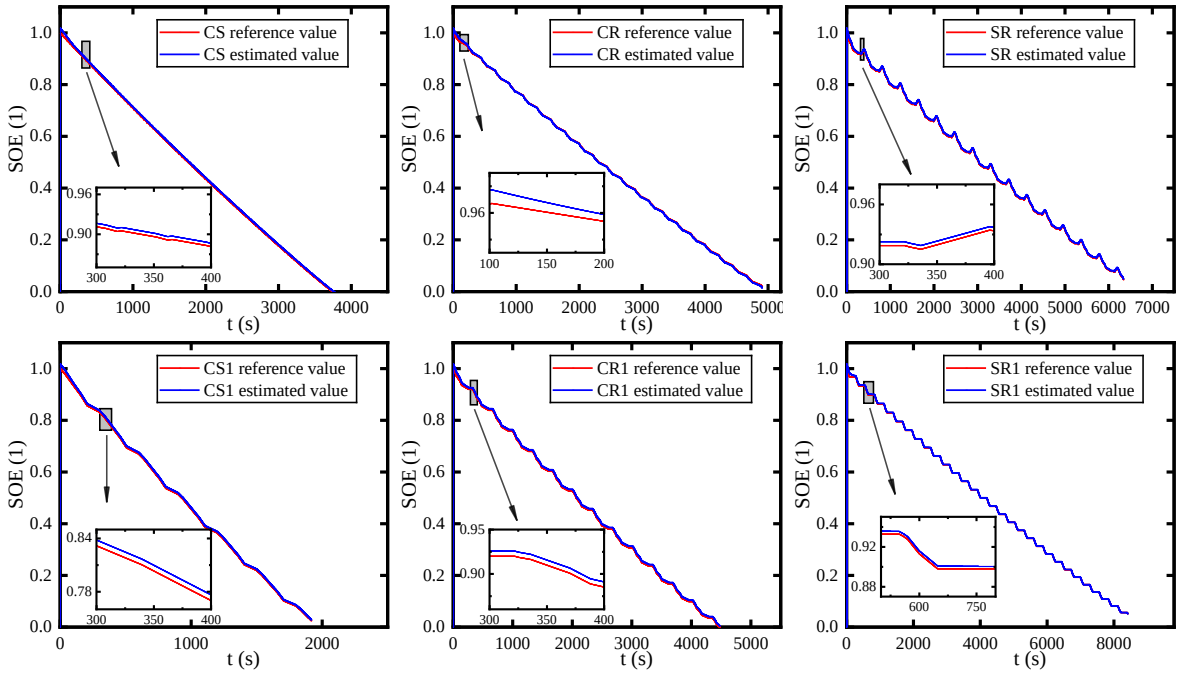

Fig. 4. (b) SOE and maximum available energy co-estimation results under 5 ℃

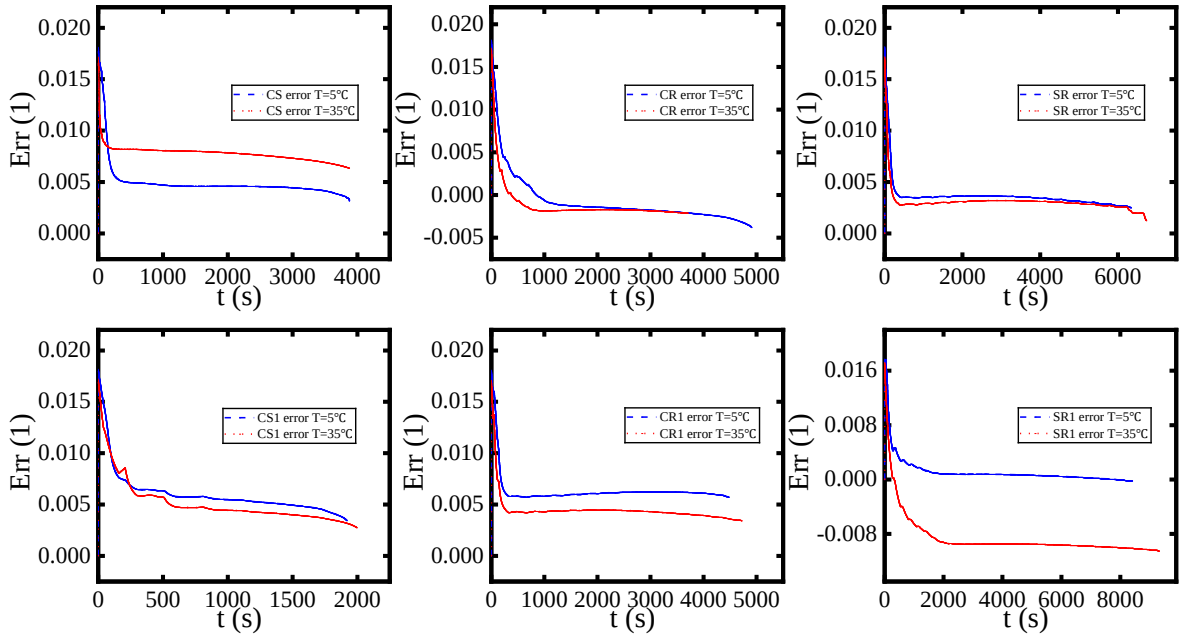

Fig.4. (c) SOE and maximum available energy co-estimation error

Fig.4 (a) and Fig.4 (b) show co-estimation results of the maximum available energy values E_n and SOE for T=35 °C and T=5 °C respectively. The results show that the predicted SOE results for each operating condition

at different temperatures follow the dynamics of the reference SOE values very well, and the initial estimates for each SOE deviate from the reference values at the beginning of the forecast due to the large errors in the initial maximum available energy values. With the effective correction of the maximum available energy values, the SOE estimate gradually moves closer to the reference values and the errors decrease.

Fig.4 (c) illustrates that the error ranges of the predicted and reference SOE curves for operating conditions CS, CS1, CR, CR1, SR and SR1 at T=35 ℃ are 0.6% to 1.71%, 0.25% to 1.72%, -0.2% to 1.72%, 0.3% to 1.71%, 0.1% to 1.68%, and -1.05% to 1.67%, respectively. At T=5 ℃, the error ranges of the predicted SOE curve and the reference SOE curve for operating conditions are 0.3% to 1.81%, 0.32% to 1.82%, -0.4% to 1.82%, 0.5% to 1.8%, 0.24% to 1.81%, and -0.37% to 1.77%, respectively. The maximum error of the working conditions at each temperature does not exceed 2%, demonstrating the correctness and effectiveness of the joint algorithm framework at this time scale.

(2) L=30

Set the micro time scale to 1 s and the macro time scale to 30 s, that is, select the time scale L=30 to update the maximum available energy. Fig. 5 shows the SOE and maximum available energy co-estimation results and their estimation errors under different operating temperatures with L=30.

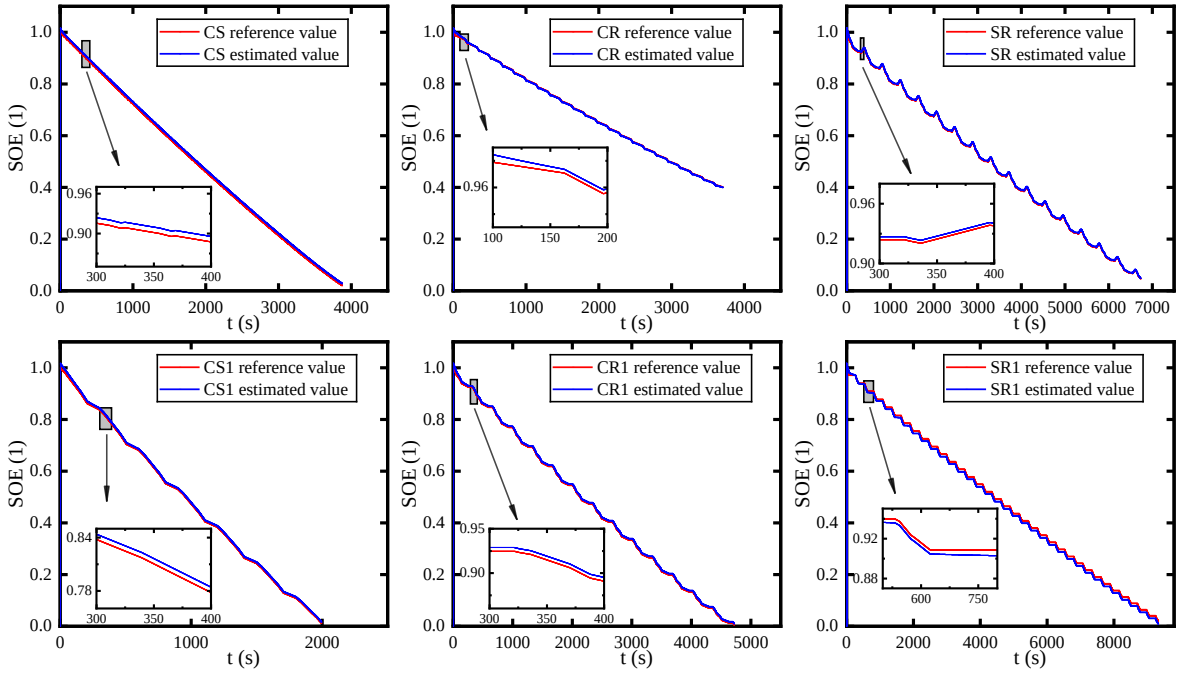

Fig. 5. (a) SOE and maximum available energy co-estimation results under 35 ℃

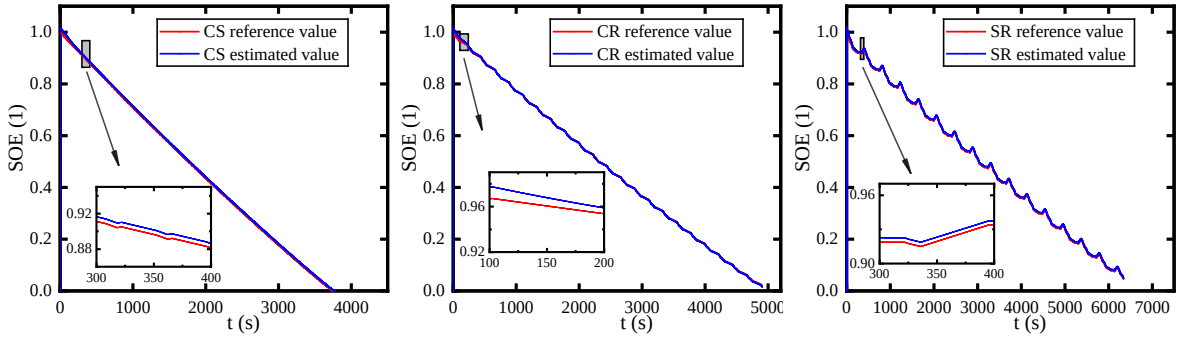

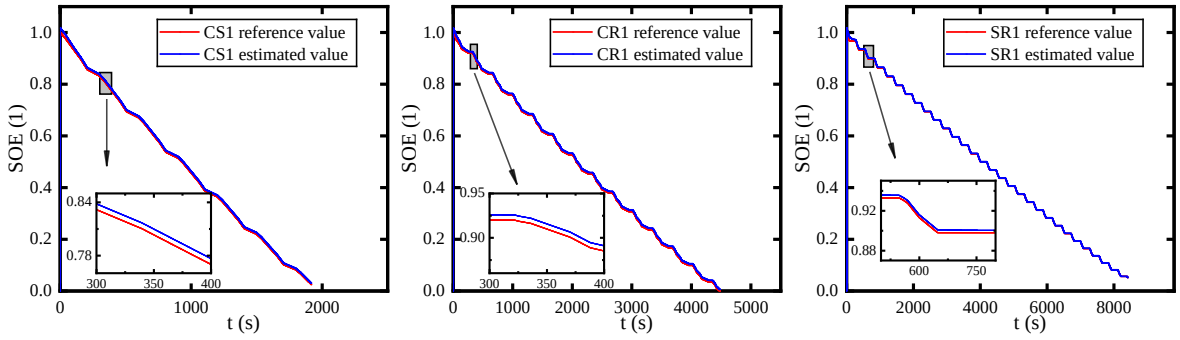

Fig. 5. (b) SOE and maximum available energy co-estimation results under 5 ℃

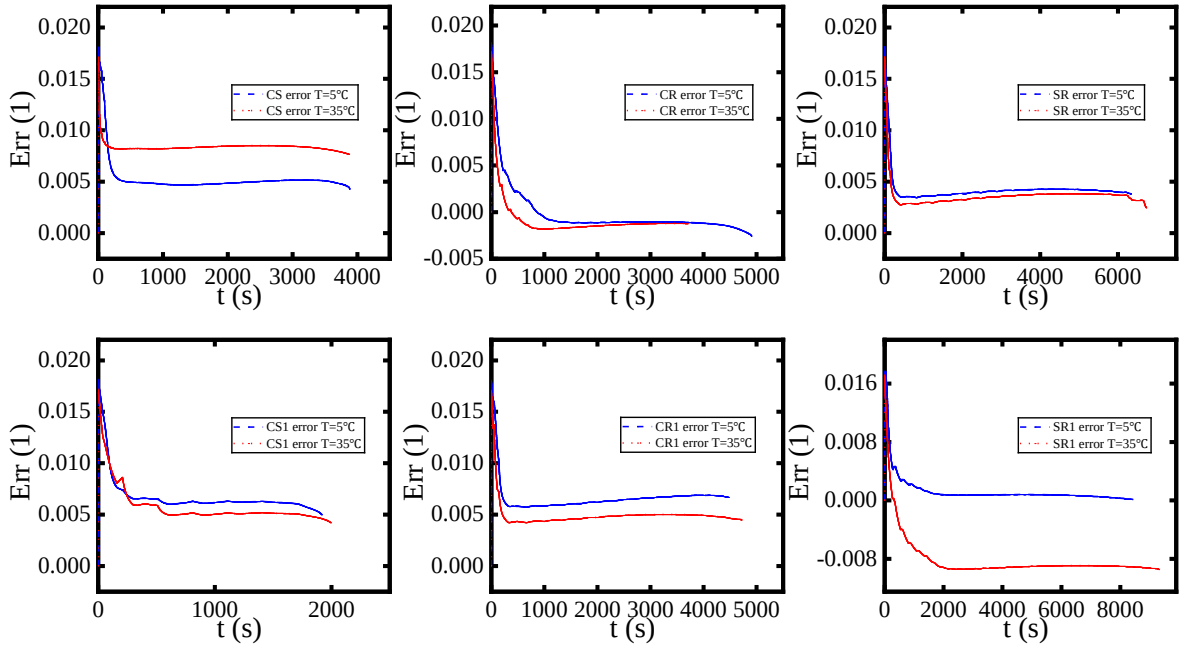

Fig. 5. (c) SOE and maximum available energy co-estimation error

Fig.5 (a) and Fig.5 (b) show that the SOE results for different temperatures of the working condition follow the reference value well at the time scale, but there is also a situation where the accuracy of SOE estimation is not high in the early stage of prediction. As the fourth-order AEKF algorithm is used to update the threshold of the maximum available energy, the SOE estimation value gradually approaches the reference value. In the middle and later stages of discharge, the predicted SOE value can better follow the change of the reference value. Fig.5 (c) represents a comparison of the results error under operating conditions of T=35 ℃ and T=5 ℃. At T=35 ℃, The error ranges of the predicted SOE curves and the reference SOE curves for the working conditions CS, CS1, CR, CR1, SR, and SR1 are 0.76% to 1.69%, 0.4% to 1.7%, -0.1% to 1.69%, 0.41% to 1.68%, 0.2% to 1.68%, and -0.95% to 1.66%, respectively. When T=5 ℃, the error ranges for the predicted SOE and reference SOE curves are 0.41% to 1.79%, 0.49% to 1.82%, -0.26% to 1.78%, 0.57% to 1.78%, 0.38% to 1.79%, 0.14% to 1.75%, with none of the maximum errors for the operating conditions exceeding 2% at each temperature, indicating the correctness and validity of the framework at this time scale.

(3) L=100

Set the micro time scale to 1 s and the macro time scale to 100 s, that is, select the time scale L=100 to update

the maximum available energy. Fig. 6 shows the SOE and maximum available energy co-estimation results and their estimation errors under different operating temperatures with L=100.

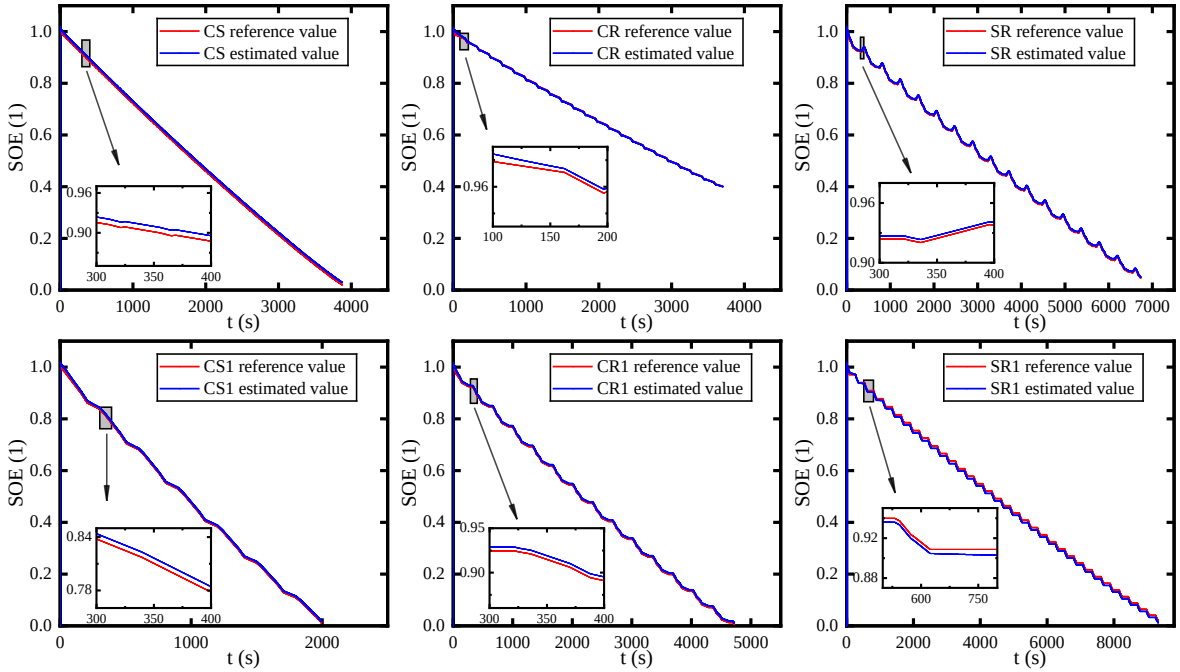

Fig. 6. (a) SOE and maximum available energy co-estimation results under 35℃

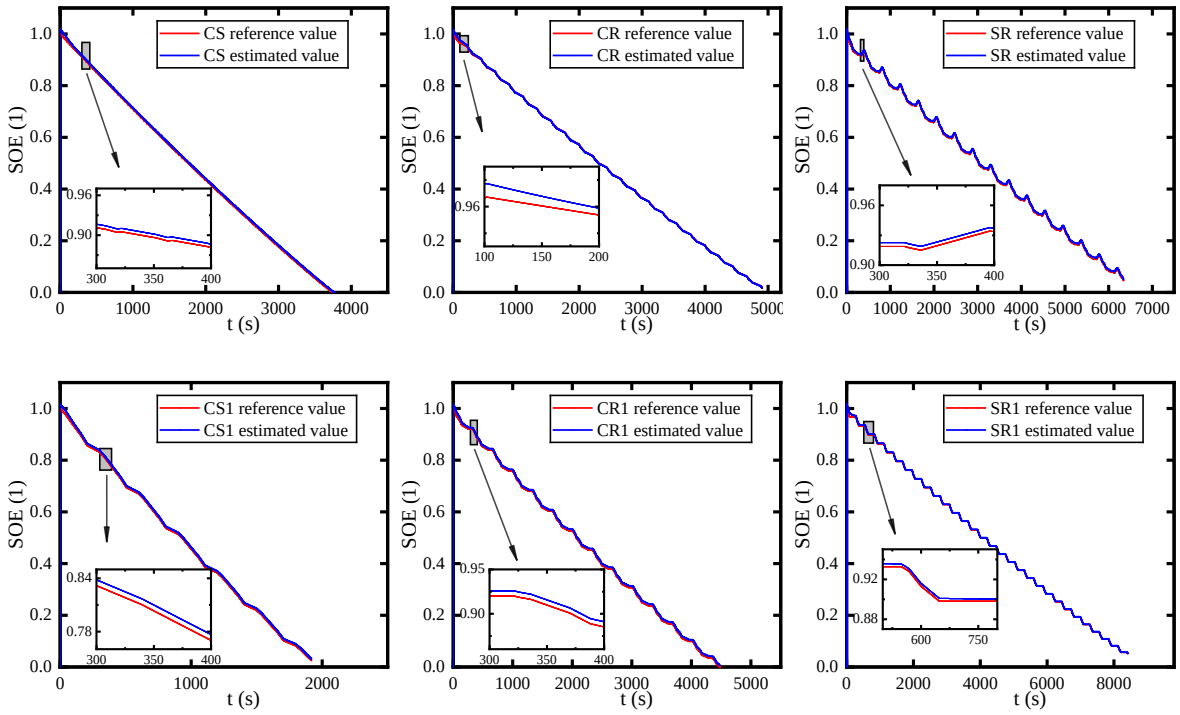

Fig. 6. (b) SOE and maximum available energy co-estimation results under 5 ℃

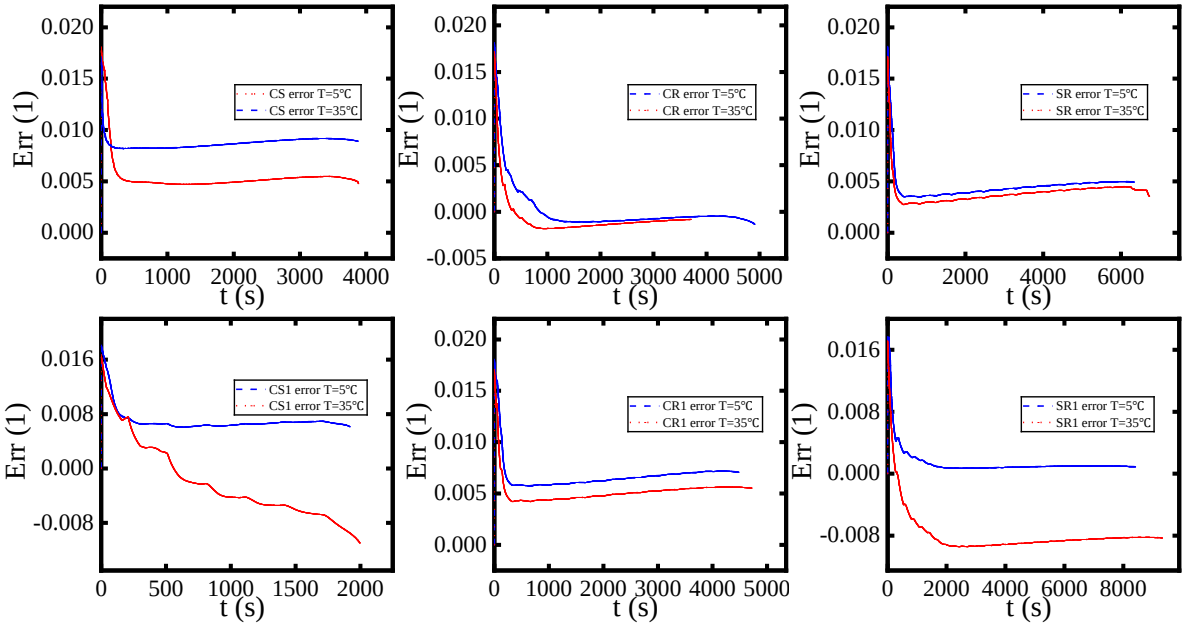

Fig. 6. (c) SOE and maximum available energy co-estimation error

Fig.6 (a) and Fig.6 (b) illustrate that when the time scale L is selected to a larger value, the co-estimation results of the maximum available energy and SOE under different temperatures can also follow the dynamic changes of the reference SOE, proving that the proposed time scale algorithm has good adaptability. However, when choosing a larger time scale, the distance between the estimated SOE deviation from the reference value will be larger compared to a smaller time scale, indicating that a larger time scale will reduce the accuracy of SOE estimation. Fig.6 (c) represents a comparison of SOE results error for the joint estimation framework at T=35 ℃ and T=5 ℃. At T=35 ℃, the error ranges of the predicted SOE curves and reference SOE curves for operating conditions CS, CS1, CR, CR1, SR, and SR1 are 0.8% to 1.65%, -1.1% to 1.66%, -0.18% to 1.68%, 0.41% to 1.67%, 0.27% to 1.69%, and -0.94% to 1.68%, respectively. At T=5 ℃, the error ranges of the predicted SOE curve and the reference SOE curve for operating conditions are 0.48% to 1.78%, 0.58% to 1.8%, -0.14% to 1.78%, 0.57% to 1.79%, 0.35% to 1.8%, and 0.1% to 1.76%, with none of the maximum errors for the working conditions exceeding 2%, indicating that a larger time scale can also ensure the correctness and effectiveness of the proposed calculation method.

The comparison of error results for different time scales at T=35 ℃ and T=5 ℃ further explains the impact of different time scale choices on the co-estimation accuracy error of maximum available energy and SOE. The experimental results show that the multi-timescale framework for various operating conditions at different temperatures can quickly eliminate the error impact caused by inaccurate initial maximum available energy, and can better track the reference SOE changes after algorithm convergence. The multi-timescale framework can effectively track the large deviation of energy values in the initial and end stages of discharge, and there is no significant deviation in the entire discharge cycle and all operating conditions, indicating that the estimation framework has good convergence and robustness. The smaller the time scale selection for most operating conditions, the lower the co-estimation error of the maximum available energy and SOE. The error will continue to increase with the increase of time scale, and a larger time scale seems to reduce the estimation accuracy of

SOE because a longer time scale means that it takes longer intervals to update the maximum available energy. As a result, the accuracy of the SOE prediction according to the collaborative estimation framework may be reduced when incorrect maximum available energy values are not corrected promptly, further affecting the correction performance of the maximum available energy values. Tab. 2 shows the root mean square error (RMSE) of SOE estimation results with macro time scales under different operating temperatures.

Tab. 2 The RMSE (%) of SOE estimation results under different operating temperatures with different time-scales

Time scale / Condition	T=5℃			T=35℃		
	L=10	L=30	L=100	L=10	L=30	L=100
CS	0.53	0.56	0.57	0.78	0.84	0.87
CS1	0.64	0.7	0.73	0.56	0.61	0.63
CR	0.3	0.27	0.26	0.26	0.24	0.23
CR1	0.65	0.68	0.69	0.46	0.51	0.53
SR	0.39	0.45	0.47	0.33	0.38	0.4
SR1	0.23	0.24	0.25	0.92	0.87	0.84

Tab. 2 shows that the SOE error range of node operating conditions can be controlled within 1% at different time scales and temperatures, indicating the effectiveness and robustness of the algorithm. Intuitively, the smallest estimation error can be obtained at the shortest time scale since the maximum available energy can be corrected in time under most operating conditions. However, the CR and SR1 operating conditions indicate that a larger time scale does not necessarily reduce the accuracy of SOE estimation, as the maximum available energy of the operating conditions varies less under long-term time scale selection. The algorithm can better track the changes in maximum available energy on the time scale, resulting in a decrease in SOE error. With the elaboration of the above results, the conclusion that the accuracy of SOE predictions is improved compared to shorter time scales is obtained.

The experimental results show that lithium-ion battery is more sensitive to high-rate discharge and low-temperature working environment, especially high-rate discharge will seriously affect the maximum available energy. Therefore, lithium-ion batteries should be avoided in the low SOE range to ensure safety and stability in the working environment. At the same time, an appropriate discharge rate should be adopted according to the ambient temperature to supply energy to the load and extend the working time of WSN nodes to the maximum extent. When the ambient temperature is high, high energy output can be obtained by using high-rate discharge. When the temperature is low, a lower discharge rate should be used to maximize the discharge energy of the battery and extend the working time of the node.

5.2. Comparison prediction results of maximum available energy

The initial maximum available energy is mistakenly set to 80% of the rated energy value in the experiment, and the energy attenuation caused by temperature and discharge rate is simulated to verify the convergence and robustness of the algorithm. Fig. 7 shows the maximum available energy variation with different macro time scales under six operating conditions at 35°C and 5°C, respectively.

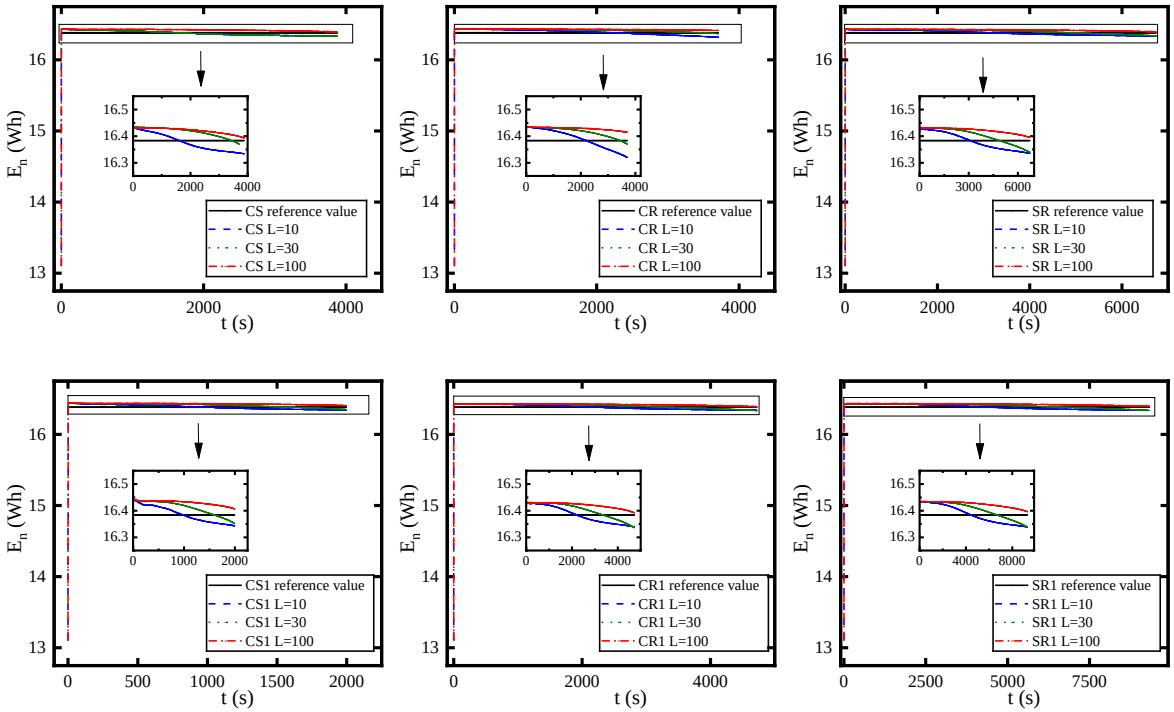

Fig. 7. (a) Maximum available energy estimation results under 35 ℃ operating temperature with different time-scales

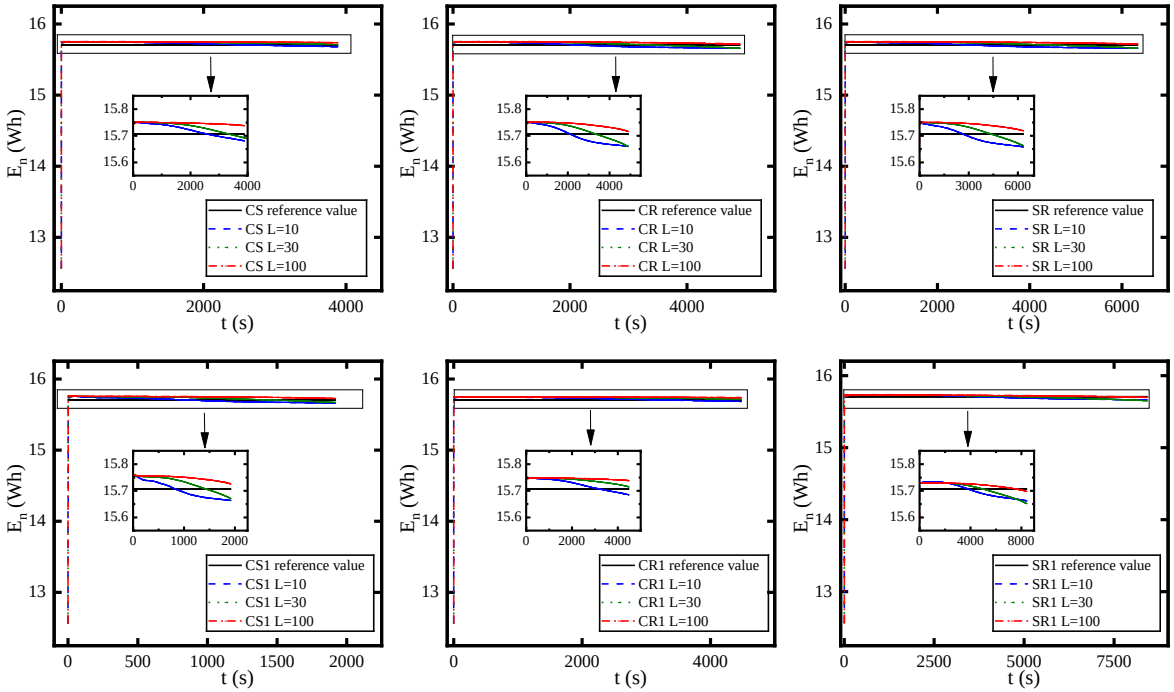

Fig. 7. (b) Maximum available energy estimation results under 5 ℃ operating temperature with different time-scales

The results indicate that the initial maximum available energy error can quickly converge to the vicinity of the reference maximum available energy through the AEKF algorithm. The initial maximum available energy under different time scales can converge to the reference maximum available energy in multiple iterations. A smaller time scale can provide more accurate and reliable maximum available energy correction. When the macro time scale is 100, the deviation between the estimated curve and the reference maximum available energy is larger due to the larger error of ΔSOE. Conversely, smaller macro time scales can provide a more accurate and reliable correction of the maximum available energy. Tab. 3 summarizes the RMSE between the maximum available

energy and the reference under different operating temperatures with different time scales, further explaining the effect of multi-timescale on prediction accuracy.

Tab. 3 The RMSE (%) of maximum available energy under different operating temperatures with different time-scales

Time scale / Condition	T=5℃			T=35℃		
	L=10	L=30	L=100	L=10	L=30	L=100
CS	2.65	3.4	4.07	3.24	3.29	3.88
CS1	2.99	3.33	4.26	2.98	3.73	4.74
CR	3.21	3.16	3.68	3.53	3.68	4.51
CR1	2.58	3.36	3.92	3.09	3.34	3.84
SR	3.09	3.06	3.66	3.13	3.31	3.9
SR1	2.58	2.38	1.73	3.32	3.55	4.2

Tab. 3 illustrates that smaller macro time scales can provide more accurate and reliable maximum available energy corrections and higher SOE estimation accuracy. Conversely, increasing the time scale will bring about a faster change in the maximum available energy, and bringing in wrong values will significantly reduce the SOE accuracy predictions. Due to the increased shelving time under SR1 working conditions, long-term shelving will improve the prediction accuracy of the terminal voltage, and there is a process of maximum available energy falling back, reducing the error between the actual available energy and the reference energy. Therefore, choosing a longer time scale for this working condition has a better energy tracking effect, which improves the SOE prediction accuracy compared to shorter time scales. The improvement of SOE accuracy further promotes the correction of the maximum available energy and reduces the RMSE. Tab. 4 summarizes the computational time of multi-timescale co-estimation framework with different macro timescales under different temperatures.

Tab. 4 The statistical results of running time (s) under different temperatures with different time-scales

operating condition	T=5℃			T=35℃		
	L=10	L=30	L=100	L=10	L=30	L=100
CS	156.8	146.38	134.35	188.6	174.8	170.8
CS1	60.38	52.36	36.26	72.49	66.64	62.96
CR	234.08	226.21	217.76	191.5	169.6	166.7
CR1	277.85	275.05	193.97	348.9	336.1	304.6
SR	403.2	397.72	380.25	488.79	473.97	447.04
SR1	569.39	547.44	544.66	685.91	664.2	658.53

Tab 4 indicates that the total running time significantly decreases with the increase of the time scale. The larger the time scale, the lower the total running time. When the time scale is selected as 100, the algorithm has the lowest time complexity. In addition, the total running time for the operating condition at T=5 °C is significantly lower than the total running time at T=35 °C, as the lower temperature leads to more energy loss from the lithium-ion batteries and the total energy that the battery can release decreases rapidly. The rapid increase in charge transfer impedance within the battery at low temperatures results in the battery reaching the cut-off voltage quickly and the total run time for the corresponding operating condition decreases. In addition, the CS1 condition has a higher operating current and longer discharge time than the rest of the conditions. The high rate

of long discharges leads to an increase in energy loss, causing the battery to quickly reach the discharge cut-off voltage and stop working, so this condition takes the least amount of time.

The multi-timescale algorithm only collects a limited amount of data for storage based on the selection of the memory length, and the collected data is automatically discarded as soon as the selection exceeds a threshold, so the algorithm has low spatial complexity. The introduction of the time scale makes the update of the maximum available energy subject to the corresponding constraints; the longer the time scale is selected, the lower the time cost spent on the algorithm. In the actual operation of WSN nodes, the choice of the appropriate time scale requires a comprehensive consideration of the balance between computational cost and prediction accuracy. A smaller timescale can be chosen when the accuracy of the remaining available energy prediction is required to be high; a larger timescale needs to be chosen when the computational complexity needs to be reduced.

5.3. Comparison of SOE results with fixed maximum available energy under different temperatures

The fixed maximum energy values have been used to calculate residual energy during the operation of lithium-ion batteries, which will lead to inaccurate SOE estimation. Fig. 8 shows the SOE and fixed maximum energy co-estimation results under different operating temperatures.

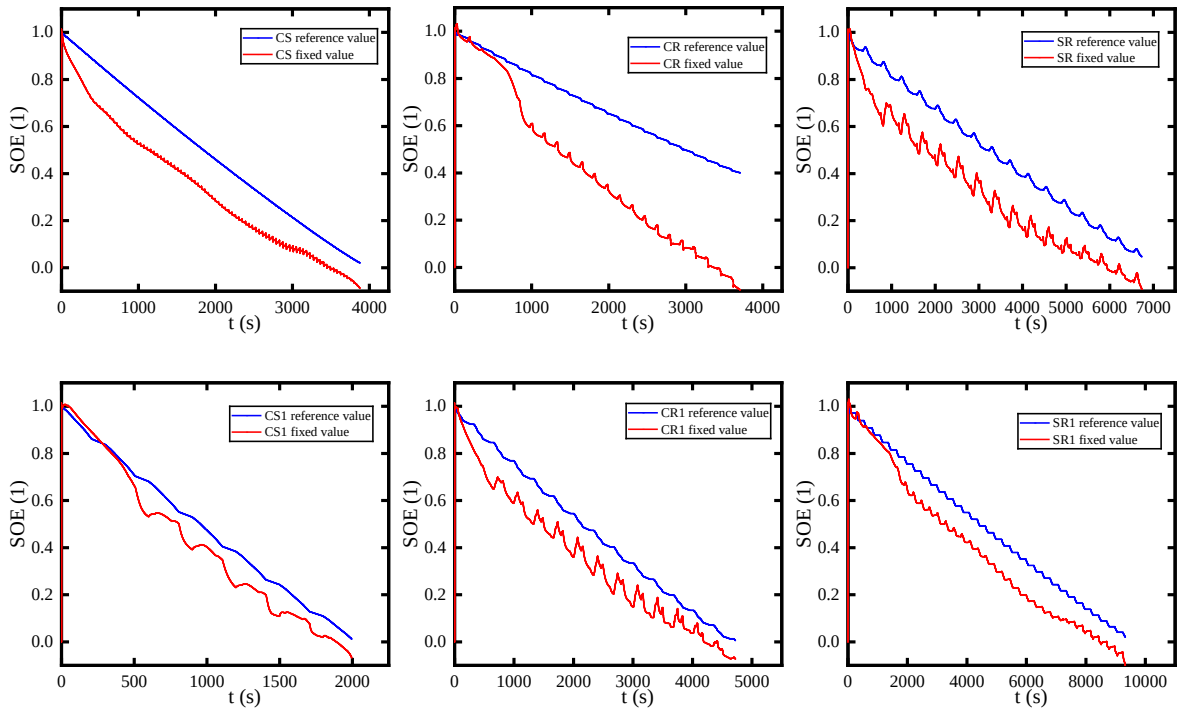

Fig. 8. (a) SOE and fixed maximum available energy co-estimation results under 35 ℃

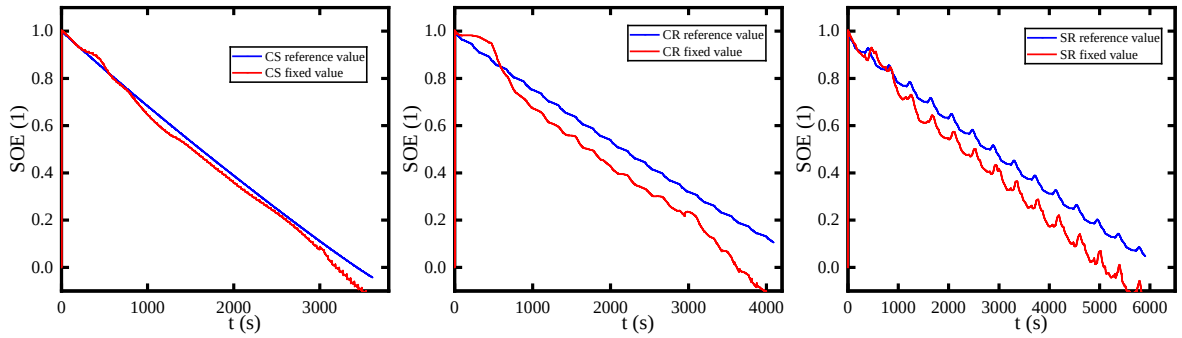

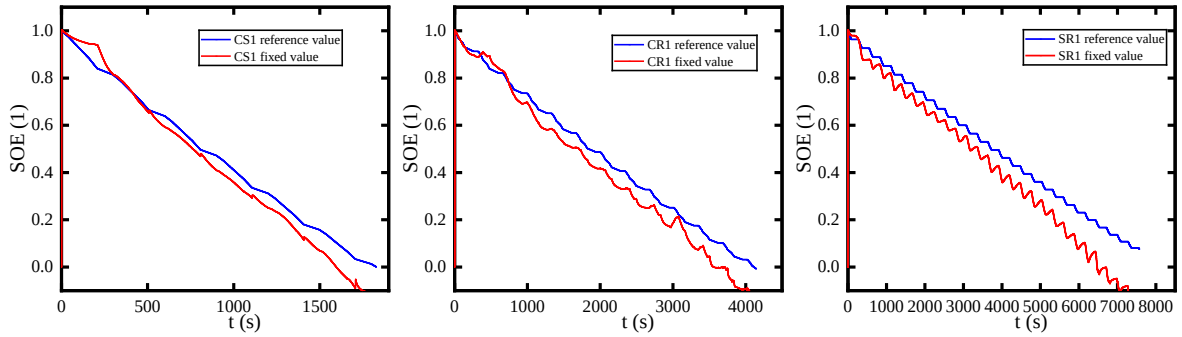

Fig. 8. (b) SOE and fixed maximum available energy co-estimation results under 5 ℃

Fig.8 (a) and Fig.8 (b) respectively show the SOE and fixed maximum energy co-estimation results under different operating temperatures. The experimental results indicate that the predicted SOE gradually deviates from the reference value in the process of battery discharge, and there is a significant deviation in the predicted results. The deviation between low temperature and high temperature predicted results is larger, indicating that the temperature loss characteristics of the maximum available energy, too high and too low temperature will cause more serious energy loss. If the fixed maximum energy is used for SOE estimation, it will cause a continuous increase in SOE error, as the dynamic range of the maximum available energy fluctuates greatly between the initial and the end of discharge. Therefore, adopting the fixed maximum energy for joint estimation will lead to a divergence of SOE prediction results.

6. Conclusions

A synergistic prediction framework for SOE and maximum available energy based on a temperature-varying FOM is proposed to ensure SOE accuracy under a wide operating temperature range, which improves the reliability of SOE in WSN. Subsequently, a multi-timescale co-estimation framework is adopted to reduce computational complexity, and the feasibility of the framework and adaptability with different macro time scales are verified through six typical operating conditions under different temperatures. The verification results show that the model can better simulate the internal reaction characteristics of the battery with the estimation error of the co-estimation framework less than 1% under different macro time scales. Furthermore, the comparison between predicted maximum available energy and fixed maximum available energy is conducted, whose results further illustrate that the necessity of the maximum available energy update and the co-estimation framework has more superior comprehensive performance on SOE accuracy. The current work mainly focuses on the basic characteristics of lithium-ion battery cells, without considering the situation of lithium-ion battery packs. Future work will focus on studying the equilibrium state of lithium-ion battery packs and their impact on state estimation. The original contribution can be summarized as:

(1). An improved co-estimation framework for SOE and maximum available energy of lithium-ion batteries in WSN nodes have been established, considering the problem of maximum available energy value decay caused by environmental temperature and battery charge-discharge rate.

(2). A multi-timescale SOE and maximum available energy co-estimation framework is proposed to address the asynchronous and coupled characteristics of maximum available energy and SOE. The micro-time scale

parameters are updated at each time step. Meanwhile, the macro-time scale parameters are only updated when the constraint conditions are satisfied, effectively reducing the algorithm's computational complexity.

(3). The experimental validation of the maximum available energy and SOE co-estimation framework under the multi-timescale is conducted according to the DST conditions. The experimental results show that the algorithm with maximum available energy correction can effectively correct the divergence problem caused by the fixed maximum available energy and significantly improve the accuracy of residual energy estimation under various working conditions.

(4). The double estimation accuracy and running time are used as indicators to evaluate the performance of the co-estimation framework under different time scales. The experimental results show that smaller time scales can provide more accurate and reliable maximum available energy correction and higher SOE estimation accuracy, but the computational time cost is higher than that of larger time scales, so the selection of time scales can achieve low time complexity and low space complexity.

7. Acknowledgments

The work is supported by the National Natural Science Foundation of China (No.62173281, No. 61801407), Natural Science Foundation of Sichuan Province (No. 2023NSFSC1436), Sichuan Science and Technology Program (No. 23NSFSC4444), and Robert Gorden University.

Reference

1 Zhang, L., Peng, H., Ning, Z., Mu, Z. & Sun, C. Comparative Research on RC Equivalent Circuit Models for Lithium-Ion Batteries of Electric Vehicles. *Appl. Sci.* **7**, 1002, doi:10.3390/app7101002 (2017).

2 She, C., Wang, Z., Sun, F., Liu, P. & Zhang, L. Battery Aging Assessment for Real-World Electric Buses Based on Incremental Capacity Analysis and Radial Basis Function Neural Network. *IEEE Transactions on Industrial Informatics* **16**, 3345-3354, doi:10.1109/tii.2019.2951843 (2020).

3 Shi, H. *et al.* On-line adaptive asynchronous parameter identification of lumped electrical characteristic model for vehicle lithium-ion battery considering multi-time scale effects. *J. Power Sources* **517**, 230725, doi:10.1016/j.jpowsour.2021.230725 (2022).

4 Dang, X. *et al.* Open-Circuit Voltage-Based State of Charge Estimation of Lithium-ion Battery Using Dual Neural Network Fusion Battery Model. *Electrochim. Acta* **188**, 356-366, doi:10.1016/j.electacta.2015.12.001 (2016).

5 Wang, Y., Zhang, X., Liu, C., Pan, R. & Chen, Z. Multi-timescale power and energy assessment of lithium-ion battery and supercapacitor hybrid system using extended Kalman filter. *J. Power Sources* **389**, 93-105, doi:10.1016/j.jpowsour.2018.04.012 (2018).

6 Liu, C. *et al.* A new method of modeling and state of charge estimation of the battery. *J. Power Sources* **320**, 1-12, doi:10.1016/j.jpowsour.2016.03.112 (2016).

7 Li, J. *et al.* Joint estimation of state of charge and state of health for lithium‐ion battery based on dual adaptive extended Kalman filter. *Int. J. Energy Res.* **45**, 13307-13322, doi:10.1002/er.6658 (2021).

8 Wang, J., Zhang, L., Mao, J., Zhou, J. & Xu, D. Fractional Order Equivalent Circuit Model and SOC Estimation of Supercapacitors for Use in HESS. *IEEE Access* **7**, 52565-52572, doi:10.1109/access.2019.2912221 (2019).

9 Zhang, Q. *et al.* A Fractional-Order Kinetic Battery Model of Lithium-Ion Batteries Considering a Nonlinear Capacity. *Electronics* **8**, doi:10.3390/electronics8040394 (2019).

10 Hidalgo-Reyes, J. I., Gomez-Aguilar, J. F., Escobar-Jimenez, R. F., Alvarado-Martinez, V. M. & Lopez-Lopez, M. G. Classical and fractional-order modeling of equivalent electrical circuits for supercapacitors and batteries,

energy management strategies for hybrid systems and methods for the state of charge estimation: A state of the art review. *Microelectronics Journal* **85**, 109-128, doi:10.1016/j.mejo.2019.02.006 (2019).

11 Xu, Y. *et al.* State of charge estimation for lithium-ion batteries based on adaptive dual Kalman filter. *Applied Mathematical Modelling* **77**, 1255-1272, doi:10.1016/j.apm.2019.09.011 (2020).

12 Chang, J., Chi, M. & Shen, T. Model based state-of-energy estimation for LiFePO4 batteries using unscented particle filter. *J. Power Electron.* **20**, 624-633, doi:10.1007/s43236-020-00051-5 (2020).

13 Wang, Y., Yang, D., Zhang, X. & Chen, Z. Probability based remaining capacity estimation using data-driven and neural network model. *J. Power Sources* **315**, 199-208, doi:10.1016/j.jpowsour.2016.03.054 (2016).

14 Ma, L., Hu, C. & Cheng, F. State of Charge and State of Energy Estimation for Lithium-Ion Batteries Based on a Long Short-Term Memory Neural Network. *Journal of Energy Storage* **37**, 102440, doi:10.1016/j.est.2021.102440 (2021).

15 Dong, G., Chen, Z., Wei, J., Zhang, C. & Wang, P. An online model-based method for state of energy estimation of lithium-ion batteries using dual filters. *J. Power Sources* **301**, 277-286, doi:10.1016/j.jpowsour.2015.10.011 (2016).

16 Shrivastava, P., Kok Soon, T., Bin Idris, M. Y. I., Mekhilef, S. & Adnan, S. B. R. S. Combined State of Charge and State of Energy Estimation of Lithium-Ion Battery Using Dual Forgetting Factor-Based Adaptive Extended Kalman Filter for Electric Vehicle Applications. *IEEE Trans. Veh. Technol.* **70**, 1200-1215, doi:10.1109/tvt.2021.3051655 (2021).

17 Wang, Y. & Chen, Z. A framework for state-of-charge and remaining discharge time prediction using unscented particle filter. *Appl. Energy* **260**, 114324, doi:10.1016/j.apenergy.2019.114324 (2020).

18 Nian, P., Shuzhi, Z. & Xiongwen, Z. Co-estimation for capacity and state of charge for lithium-ion batteries using improved adaptive extended Kalman filter. *Journal of Energy Storage* **40**, 102559, doi:10.1016/j.est.2021.102559 (2021).

19 Ghomian, T. & Mehraeen, S. Survey of energy scavenging for wearable and implantable devices. *Energy* **178**, 33-49, doi:10.1016/j.energy.2019.04.088 (2019).

20 Ali, O. *et al.* On-line WSN SoC estimation using Gaussian Process Regression: An Adaptive Machine Learning Approach. *Alexandria Engineering Journal* **61**, 9831-9848, doi:10.1016/j.aej.2022.02.0671110-0168 (2022).

21 Aoudia, F. A., Gautier, M. & Berder, O. RLMan: An Energy Manager Based on Reinforcement Learning for Energy Harvesting Wireless Sensor Networks. *Ieee Transactions on Green Communications and Networking* **2**, 408-417, doi:10.1109/tgcn.2018.2801725 (2018).

22 Zheng, L., Zhu, J., Wang, G., He, T. & Wei, Y. Novel methods for estimating lithium-ion battery state of energy and maximum available energy. *Appl. Energy* **178**, 1-8, doi:10.1016/j.apenergy.2016.06.031 (2016).

23 Zhang, S., Peng, N. & Zhang, X. A variable multi‐time‐scale based dual estimation framework for state‐of‐energy and maximum available energy of lithium‐ion battery. *Int. J. Energy Res.* **46**, 2876-2892, doi:10.1002/er.7350 (2021).

24 Tang, X., Wang, Y., Yao, K., He, Z. & Gao, F. Model migration based battery power capability evaluation considering uncertainties of temperature and aging. *J. Power Sources* **440**, 227141, doi:10.1016/j.jpowsour.2019.227141 (2019).

25 Liu, C., Wang, Y. & Chen, Z. Degradation model and cycle life prediction for lithium-ion battery used in hybrid energy storage system. *Energy* **166**, 796-806, doi:10.1016/j.energy.2018.10.131 (2019).

26 Tang, X. *et al.* A novel framework for Lithium-ion battery modeling considering uncertainties of temperature and aging. *Energy Convers. Manage.* **180**, 162-170, doi:10.1016/j.enconman.2018.10.082 (2019).

27 Lajara, R. J., Perez-Solano, J. J. & Pelegri-Sebastia, J. A Method for Modeling the Battery State of Charge in Wireless Sensor Networks. *IEEE Sensors Journal* **15**, 1186-1197, doi:10.1109/jsen.2014.2361151 (2015).

28 Zhang, X., Wang, Y., Wu, J. & Chen, Z. A novel method for lithium-ion battery state of energy and state of power estimation based on multi-time-scale filter. *Appl. Energy* **216**, 442-451, doi:10.1016/j.apenergy.2018.02.117

(2018).

29 Wang, Y., Li, M. & Chen, Z. Experimental study of fractional-order models for lithium-ion battery and ultra-capacitor: Modeling, system identification, and validation. *Appl. Energy* **278**, 115736, doi:10.1016/j.apenergy.2020.115736 (2020).

30 Xiong, R., Wang, J., Shen, W., Tian, J. & Mu, H. Co-Estimation of State of Charge and Capacity for Lithium-Ion Batteries with Multi-Stage Model Fusion Method. *Engineering* **7**, 1469-1482, doi:10.1016/j.eng.2020.10.022 (2021).

31 Shi, H. *et al.* A novel lumped thermal characteristic modeling strategy for the online adaptive temperature and parameter co-estimation of vehicle lithium-ion batteries. *Journal of Energy Storage* **50**, 104309, doi:10.1016/j.est.2022.104309 (2022).

32 Chen, L., Wang, S., Jiang, H. & Fernandez, C. A novel combined estimation method for state of energy and predicted maximum available energy based on fractional-order modeling. *Journal of Energy Storage* **62**, 106930, doi:10.1016/j.est.2023.106930 (2023).